Quantum control of double ionization of calcium

Maxim Sukharev,* Eric Charron, and Annick Suzor-Weiner
Laboratoire de Photopysique Moléculaire du CNRS, Université Paris-XI, Bâtiment 210, 91405 Orsay Cedex, France
(Received 25 July 2002; published 18 November 2002)

We have performed nonperturbative time-dependent calculations of single and double ionization of atomic calcium by short and intense laser pulses using a two-active-electron model. It is shown that the significant enhancement of the Ca^{2+} yield observed in a recent experiment [E. Papastathopulous, M. Strehle, and G. Gerber (unpublished)] using feedback control techniques originates from the time asymmetry of the pulse shape. Numerical simulations have been performed for various asymmetrical pulses. The initial part of the pulse prepares a coherent superposition of excited states which is transferred into the double-electron continuum at later times. An asymmetric shape, with a slowly decreasing tail, therefore favors the production of Ca^{2+}. Single-active-electron calculations have also been performed to demonstrate the significant role played by electron correlations and by doubly excited states.

DOI: 10.1103/PhysRevA.66.053407 PACS number(s): 32.80.Qk, 82.50.Nd, 32.80.Fb, 32.80.Rm

I. INTRODUCTION

Multiple ionization dynamics studies have shown that, depending on the intensity regime, direct two-electron and sequential ionization processes may occur [2,3] under strong laser irradiation. In particular, the measurement [4,5], ten years ago, of a shoulder in the double ionization yield of the He atom as a function of intensity was interpreted as an indication that direct two-electron processes can dominate double ionization at moderate intensities [6–8].

Atoms with lower ionization potentials, like alkaline-earth-metal elements, usually show a more complex ionization dynamics since single and double ionization can be in competition at relatively low intensities. Early experimental studies on the Calcium atom for example [9,10] have shown that intermediate resonances may influence significantly the ionization dynamics, and that, even if sequential ionization usually dominates the production of doubly charged ions, electron correlations play an important role, even for single ionization.

More recently [1], feedback control experiments have been performed to determine the conditions required to enhance double ionization. These experiments follow the original ideas of *optimal control theory* [11–13], later extended by Judson and Rabitz [14] into an hypothetical experimental setup able to solve and control the Schrödinger equation exactly and in real time. Shortly afterwards, this approach has proven to be very effective in real experimental conditions [15–17] using a feedback which automatically adapts the laser characteristics in the quest for an optimal electric field.

In intense fields, the experimental control of the competition between single and double ionization of Calcium [1] was performed using a programmable pulse shaper which maintains the pulse energy while modifying its spectral phase components, and therefore its chirp and shape, until the best solution for the ''fitness'' function is found. A detailed description of this experimental scheme can be found in Refs. [15,18]. The maximization of the double ionization yield was achieved for a specific electric field, from which we try, in this article, to extract the main features responsible for the optimization.

Section II presents the numerical method used here in order to follow the single and double ionization dynamics of Ca, while our main results are presented in Sec. III. A brief conclusion, Sec. IV, summarizes our results.

II. NUMERICAL METHOD

A. Two-electron model

In intense fields with linear polarization, the electronic motion is mainly confined along the direction of the electric field, and we therefore restrict our calculation to one-dimension only. The model atom which results from this restriction cannot be expected to represent faithfully the real atomic Ca, but we show, by comparison with experimental results, that this approximation is accurate enough to bring some physical insight into the dynamics of ionization with intense and linearly polarized laser pulses. We also restrict the number of active electrons in our model to the two electrons of the outer shell $n=4$. The system under consideration thus consists in two electrons and a fixed nucleus of charge $Z=+2$, interacting through a screened Coulomb potential [see, e.g., Ref. [19] for an overview]. The Hamiltonian of this one-dimensional atom can be written in the following form (if not indicated differently, atomic units are used throughout the paper)

$$H_0(x_1,x_2)=T_1+T_2+V(x_1)+V(x_2)+V_{12}(|x_2-x_1|), \tag{1}$$

where x_i $(i=1,2)$ denote the positions of the two electrons, and

$$T_i=-\frac{1}{2}\frac{\partial^2}{\partial x_i^2} \tag{2}$$

are their kinetic energy operators. The interaction energy between the ith electron and the nucleus is taken as a smoothed Coulomb potential

*Electronic address: Maxim.Sukharev@ppm.u-psud.fr

$$V(x_i) = -\frac{2}{\sqrt{\alpha^2 + x_i^2}}, \tag{3}$$

as well as the electron-electron interaction

$$V_{12}(|x_2 - x_1|) = \frac{1}{\sqrt{\beta^2 + (x_2 - x_1)^2}}. \tag{4}$$

The two smoothing parameters α and β are chosen ($\alpha = 3.894\,90$ a.u., $\beta = 3.963\,05$ a.u.) such that the energies of the ground electronic states of Ca and Ca^+ equal their ionization potentials ($V_{\text{ion}}^1 = 6.1126$ eV, $V_{\text{ion}}^2 = 11.8725$ eV).

B. Basis set representation

In order to obtain the stationary states $\psi_n(x_1, x_2)$ of the field-free Hamiltonian (1), we solve the two-particle time-independent Schrödinger equation

$$H_0 \psi_n(x_1, x_2) = E_n \psi_n(x_1, x_2) \tag{5}$$

using a basis set representation.

We first obtain the one-electron wave functions $\varphi_k(x)$ which are solutions of the equation

$$\left(-\frac{1}{2}\frac{d^2}{dx^2} - \frac{2}{\sqrt{\alpha^2 + x^2}} \right) \varphi_k(x) = \varepsilon_k \varphi_k(x). \tag{6}$$

To solve this last equation, we use the so-called mapped Fourier grid method [20–22]. Let us introduce the new mapped coordinate $p(x)$:

$$p(x) = \frac{1}{\pi} \int_{x_0}^{x} \sqrt{-V(x')}\, dx', \tag{7}$$

where x_0 is the left grid boundary (-100 a.u. in the present calculation). The integral (7) has an analytical form for a smoothed Coulomb potential (see the Appendix A for details). The coordinate transformation (7) is useful with a long-range potential (like the Coulomb interaction) because it ''compresses'' the grid at large distances. Figure 1 illustrates this effect: with a constant grid step δp in the mapped space, many points are located near $x = 0$, while the density of points decreases at large distances. Indeed, within this approach, the variable grid step δx happens to be simply proportional to the local de Broglie wavelength. For convergence, we use an x range of 200 a.u. (-100 a.u. $\leqslant x \leqslant 100$ a.u.), with 300 points. When diagonalizing the associated Fourier grid Hamiltonian [20], we obtain $N = 93$ one-electron wave functions φ_k at an energy $\varepsilon_k < 1$ a.u.

These one-electron wave functions are then used to construct a basis set of two-electron noninteracting states $\Phi_m(x_1, x_2)$. These spatial wave functions must be either symmetric (if singlet) or antisymmetric (if triplet) with respect to the exchange of the two indistinguishable electrons ($x_1 \leftrightarrow x_2$). In the absence of orbital motion (1D model), there is no spin-orbit coupling, so all spin quantum numbers are conserved. Throughout this work we shall assume the electron spins to be antiparallel, and thus restrict our calculations to singlet electronic states only. Therefore, we consider only the symmetric combinations

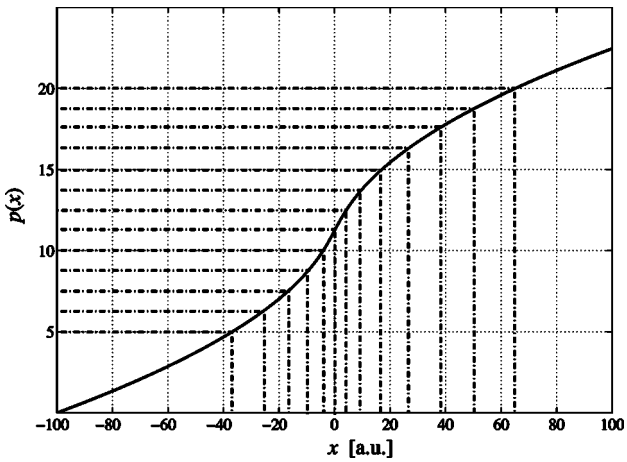

FIG. 1. Mapped coordinate $p(x)$ defined in Eq. (7) as a function of the electron coordinate x in a.u. The smoothing parameter of the screened Coulomb potential is $\alpha = 3.894\,90$ a.u.

$$\Phi_m(x_1, x_2) = \begin{cases} \dfrac{1}{\sqrt{2}}(|k_1 l_2\rangle + |k_2 l_1\rangle) & \text{if } k \neq l \\ |k_1 k_2\rangle & \text{otherwise,} \end{cases} \tag{8}$$

where we have used the following compact Dirac notations for the one-electron wave functions solutions of Eq. (6):

$$\varphi_k(x_i) \equiv |k_i\rangle. \tag{9}$$

From the $N = 93$ one-electron eigenstates obtained previously, $N(N+1)/2 = 4371$ basis functions $\Phi_m(x_1, x_2)$ are obtained.

We then construct the matrix representation of the Hamiltonian (1) in the basis set (8), as discussed in the Appendix B. After diagonalizing this matrix we obtain the solutions of the Schrödinger equation (5) as

$$\psi_n(x_1, x_2) = \sum_m A_m^{(n)} \Phi_m(x_1, x_2). \tag{10}$$

The slowest step in the calculation of these eigenstates is the construction of the matrix representing H_0, since it requires the evaluation of two-dimensional integrals. However, taking into account another symmetry property of the system can enhance significantly the efficiency of the calculation. Indeed, the Hamiltonian H_0 is invariant when changing (x_1, x_2) for $(-x_1, -x_2)$. As a consequence, one can separate the Hilbert space into two uncoupled subspaces of distinct symmetry: the symmetric or *gerade g* and the antisymmetric or *ungerade u* subspaces. Finally, we obtain a discretized set of eigenstates of H_0 which, in a first approximation, can be interpreted as bound, singe-electron continuum and double-electron continuum states, as listed in Table I. Note that the

TABLE I. Number of *gerade* N_g and *ungerade* N_u bound (a), single-electron continuum (b), and double-electron continuum states (c) calculated when diagonalizing H_0. E_1 is the ground-state energy.

	N_g	N_u	States of energy E_n
(a)	9	8	$E_1<E_n<E_1+V^1_{\rm ion}$
(b)	203	193	$E_1+V^1_{\rm ion}<E_n<E_1+V^1_{\rm ion}+V^2_{\rm ion}$
(c)	1574	1552	$E_1+V^1_{\rm ion}+V^2_{\rm ion}<E_n<1$ a.u.

number N_g of *gerade* states is higher than the number N_u of *ungerade* states because the products $|k_1k_2\rangle$ in Eq. (8) are necessarily symmetric.

C. Laser interaction

The dynamics of the system in an external linearly polarized laser field is described by the time-dependent Schrödinger equation

$$i\frac{\partial}{\partial t}\Psi(x_1,x_2,t)=[H_0-\mu E(t)]\Psi(x_1,x_2,t), \qquad (11)$$

where $\mu=-(x_1+x_2)$ is the two-electron dipole moment, and $E(t)$ the time-dependent electric field.

Let us expand the wave packet $\Psi(x_1,x_2,t)$ over the eigenfunctions $\psi_n(x_1,x_2)$:

$$\Psi(x_1,x_2,t)=\sum_n c_n(t)e^{-iE_nt}\psi_n(x_1,x_2). \qquad (12)$$

Introducing this expansion into Eq. (11), and taking into account the fact that the electric field only couples states of different symmetry (g with u), yields the following system of first-order ordinary differential equations for the coefficients $c_n(t)$:

$$\frac{dc_n^{(g)}}{dt}=iE(t)\sum_m c_m^{(u)}(t)e^{i(E_n^{(g)}-E_m^{(u)})t}D_{nm}^{(gu)},$$

$$\frac{dc_n^{(u)}}{dt}=iE(t)\sum_m c_m^{(g)}(t)e^{i(E_n^{(u)}-E_m^{(g)})t}D_{nm}^{(ug)}, \qquad (13)$$

where the matrix elements $D_{nm}^{(gu)}$ of the dipole moment are given by the two-dimensional integrals

$$D_{nm}^{(gu)}=\langle\psi_n^{(g)}|\mu|\psi_m^{(u)}\rangle. \qquad (14)$$

The superscripts (g) and (u) have been added here to distinguish the two different symmetries. It should be emphasized that the calculation of these matrix elements can be reduced to simple sums of one-dimensional integrals $\langle\varphi_k|x|\varphi_l\rangle$, owing to Eqs. (8) and (10) (see the Appendix C for details).

The Eqs. (13) are solved by the Runge-Kutta-Verner method [23], assuming that the atom is initially in its ground state: $c_n(t=0)=\delta_{1n}$. Since this method enables the truncation error to be estimated, the desired solution is obtained with automatic control of the step size δt.

In this approach, the eigenstates of H_0 are box-normalized (i.e., $\langle\psi_n|\psi_m\rangle=\delta_{nm}$), and the probabilities of single and double ionization at the end of the pulse ($t=t_f$) are therefore obtained as

$$W(\mathrm{Ca}^+)=\sum_{n_0<n\leqslant n_1}|c_n(t_f)|^2, \qquad (15)$$

and

$$W(\mathrm{Ca}^{2+})=\sum_{n_1<n\leqslant n_2}|c_n(t_f)|^2, \qquad (16)$$

where the index n_0 refers to the last bound state (i.e., the last state of energy $E_{n_0}<E_1+V^1_{\rm ion}$), n_1 to the last single-electron continuum state (i.e., the last state of energy $E_{n_1}<E_1+V^1_{\rm ion}+V^2_{\rm ion}$), and n_2 to the last two-electron continuum state included in the expansion (12), with the energy $E_{n_2}\simeq 1$ a.u. The probability of survival of the neutral atom is thus given by

$$\mathrm{W(Ca)}=\sum_{1\leqslant n\leqslant n_0}|c_n(t_f)|^2. \qquad (17)$$

Note that a useful convergence test can be performed by verifying that

$$\mathrm{W(Ca)}=1-\mathrm{W}(\mathrm{Ca}^+)-\mathrm{W}(\mathrm{Ca}^{2+}), \qquad (18)$$

an indication that the norm of the wave packet is well conserved.

We have assumed here that autoionizing states lying within the single-electron continuum ultimately decay to $(\mathrm{Ca}^+ + e^-)$. The typical values of the autoionization rates of alkaline-earth-metal elements [10^9-10^{14} s^{-1} [24]] justify this approximation.

The fact that we can easily separate the Ca^+ from the Ca^{2+} parts in the ionization probability is a clear advantage of the basis set representation that we have adopted compared to a grid approach. When the wave packet propagation is performed on a grid, disentangling single- from double-ionization requires the use of drastic approximations, like for instance a spatial discrimination [see, e.g., Refs. [7,25]], or requires to project the wave packet at the end of the pulse ($t=t_f$) on approximate (usually uncorrelated) continuum eigenstates [see, e.g., Ref. [26]].

III. NUMERICAL RESULTS

A. Experimentally optimized electric field

The time-dependent electric field associated with the laser pulse can be written as

$$E(t)=\sqrt{I_0}f(t)\cos[\omega t+\varphi(t)], \qquad (19)$$

where I_0 denotes the peak intensity, $f(t)$ the pulse envelope, and ω the angular frequency. The associated wavelength is $\lambda=800$ nm, corresponding to the photon energy $\hbar\omega=1.55$ eV. The time-dependent phase $\varphi(t)$ is introduced to

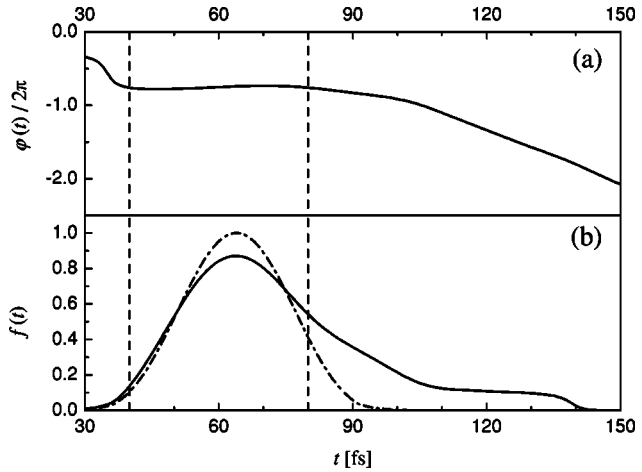

FIG. 2. Optimized electric field as a function of time t in fs, from Ref. [1] (with permission). The maximization of the Ca^{2+} signal yields the pulse shape $f(t)$ plotted as a solid line in panel (b) and the phase $\varphi(t)$ shown in panel (a). An unmodulated Gaussian shape carrying the same amount of energy is also shown as a dash-dotted line in panel (b). We have squeezed the experimental pulse shape given in Ref. [1] such that its total duration does not exceed 150 fs (see text for details). The vertical dashed lines indicate the time interval during which $\varphi(t) \simeq$ cst.

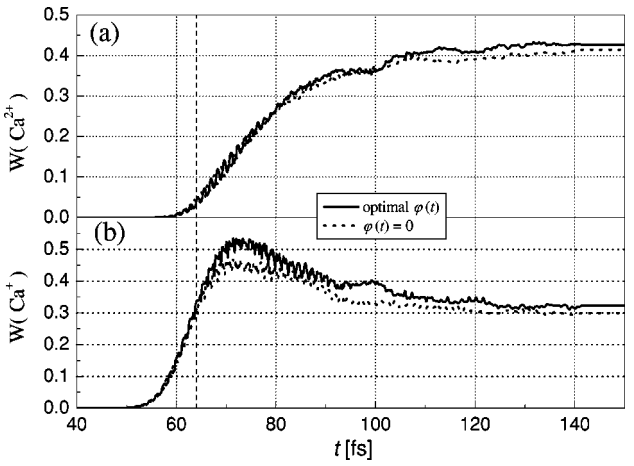

FIG. 3. Single- and double-ionization probabilities $W(Ca^{+})$ [panel (b)] and $W(Ca^{2+})$ [panel (a)] as a function of time. The optimized pulse envelope $f(t)$ of Fig. 2 has been used to calculate the ion yields with (solid lines) and without (dotted lines) the optimal phase $\varphi(t)$. The peak intensity is $I_0 = 3\times10^{12}$ W/cm^2. The vertical dashed line indicates the date of peak intensity $t_p = 64$ fs.

describe the frequency chirp of the pulse. The experiment [1] used pulse durations of about 300 fs. To keep the execution time of the numerical simulations within reasonable limits, we performed calculations for shorter pulses, with durations of the order of 150 fs. We have verified, for a restricted set of laser intensities, that increasing the pulse duration up to 300 fs does not change our main conclusions.

The pulse envelope $f(t)$ obtained in the experimental study [1] when maximizing the Ca^{2+} yield is plotted in the lower panel (b) of Fig. 2 as a solid line. This envelope can be compared with the unmodulated Gaussian pulse carrying the same amount of energy, shown as a dash-dotted line in the same figure. The main differences between the two pulse shapes are (i) their maxima, higher for the Gaussian pulse, and (ii) the long tail of the optimized pulse on the falling edge, after the peak at $t = t_p$. The asymmetry of this pulse envelope with respect to t_p, as we will show below, plays a significant role in the enhancement of the Ca^{2+} yield.

The phase $\varphi(t)$ associated with the optimized pulse shape is plotted in the upper panel (a) of Fig. 2. This phase is roughly constant (no chirp) over the interval 40 fs $\leqslant t \leqslant$ 80 fs, where the intensity is the largest. At later times ($t \geqslant 80$ fs), a negative chirp is observed.

In order to determine the influence of the chirp on the ionization dynamics, we first compare numerical simulations taking into account the optimized phase $\varphi(t)$ with calculations using an unchirped electric field, i.e., $\varphi(t) = 0$. These calculations were performed with the optimized pulse shape $f(t)$ shown in Fig. 2. Figure 3 shows a typical example of the effect of the chirp on the single- [panel (b)] and double- [panel (a)] ionization probabilities, for the intensity $I_0 = 3\times10^{12}$ W/cm^2. Until the date $t_p \simeq 64$ fs of peak intensity, the single- and double-ionization probabilities are clearly insensitive to the introduction of the optimal phase. At later times ($t \geqslant t_p$ for Ca^{+} and $t \geqslant 80$ fs for Ca^{2+}), a relatively small enhancement of single-, as well as double-ionization, is observed with the chirped pulse. In our calculation, the production of Ca^{+} is increased by about 7% with the chirp while the Ca^{2+} yield is only increased by about 3%. Introducing the chirp, therefore mainly favors single ionization, an effect which seems *a priori* in opposition with the desired goal of favoring double ionization. However, the experimental optimization was performed on the absolute Ca^{2+} yield, and not on the Ca^{2+}/Ca^{+} ratio. The small negative chirp at $t \geqslant 80$ fs slightly helps double ionization, but its effect is far from being large enough, at least in our model, to explain the experimental result, which is characterized by an increase of the Ca^{2+} yield of about 30%.

We will now look at the influence of the long tail of the optimal pulse at $t \geqslant t_p$ by comparing, in Fig. 4, the single- (solid line) and double- (dash-dotted line) ionization probabilities calculated with the two pulse shapes shown previously: the Gaussian shape in panel (a) and the optimal shape in panel (b). These calculations were performed without any chirp, i.e., $\varphi(t) = 0$. The production of the doubly charged ion dominates at intensities $I \geqslant 3.7\times10^{12}$ W/cm^2 with the Gaussian shape, while the optimal pulse already favors Ca^{2+} for $I \geqslant 2.8\times10^{12}$ W/cm^2. The enhancement of double ionization with the asymmetric shape appears to be much more significant than the increase due to the chirp. For example, at the intensity $I_0 = 2.8\times10^{12}$ W/cm^2, the single-ionization probability decreases by about 17% when changing the Gaussian shape for the optimal shape, while the double-ionization probability increases by about 35%. This last result is in good agreement with the experimental control of double ionization: +30% for Ca^{2+} [1].

The ratio Ca^{2+}/Ca^{+} is presented in Fig. 5 as a function of the peak intensity for the two pulse shapes of Fig. 2. The solid line represents the branching ratio obtained with the

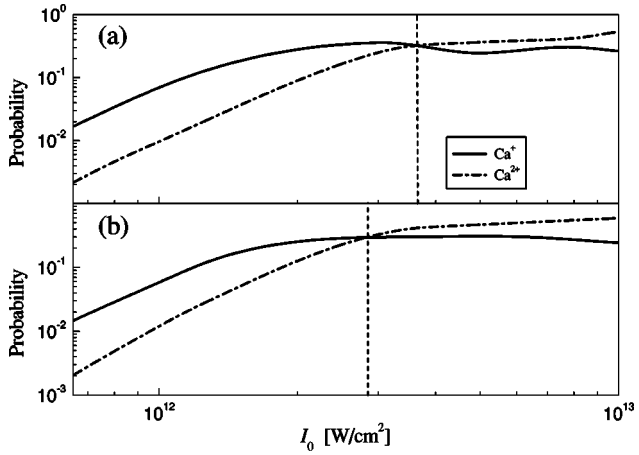

FIG. 4. Log-log representation of the single- and double-ionization probabilities $W(Ca^+)$ (solid line) and $W(Ca^{2+})$ (dash-dotted line) as functions of the peak intensity I_0 in W/cm^2 for the Gaussian (a) and the optimized (b) shapes of Fig. 2. These results were obtained assuming $\varphi(t)=0$. The two vertical dashed lines indicate the intensities at which $W(Ca^{2+})=W(Ca^+)$ for the two pulse shapes.

Gaussian pulse, while the dash-dotted line was obtained with the optimal shape. One can notice here that, at any peak intensity, the optimized shape favors the production of the doubly charged ion.

Obviously, a realistic comparison with the experiment requires averaging the ionization probabilities over the focal volume. We calculated these averaged yields assuming that the continuous distribution of intensities inside the focal volume can be described by a standard Lorentzian profile along the direction of propagation of the laser beam and a Gaussian profile in the perpendicular direction [27]. This average procedure allowed us to compare the calculated and measured single- and double-ionization yields: at low intensities (before the saturation regime), the averaged calculated Ca^+ and Ca^{2+} yields vary as I^N with $N=4.04$ for Ca^+, and $N=3.10$ for Ca^{2+}. Experimentally, the following power values have been obtained for single and double ionization: $N=4.2\pm0.7$ and $N=3.4\pm0.1$. These results are again in good agreement and indicate that the proposed two-active-electron model gives a realistic description of the single- and double-ionization dynamics of Ca in short and intense linearly polarized fields. The power law for Ca^{2+} indicates that some intermediate resonances are involved in the double-ionization process since direct double ionization of Ca would require 12 photons in order to reach the two-electron continuum.

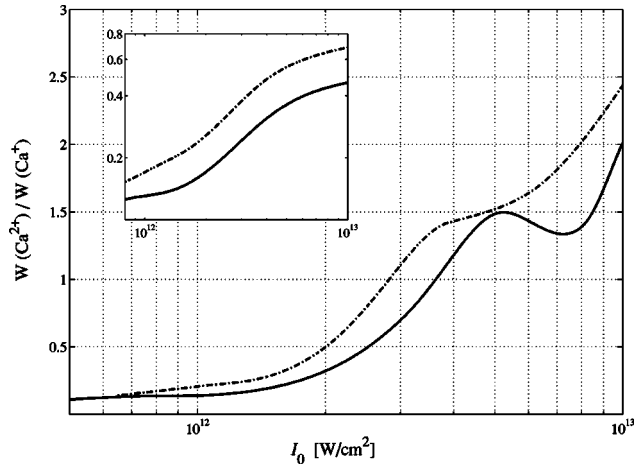

FIG. 5. Calculated double- to single-ionization branching ratios $W(Ca^{2+})/W(Ca^+)$ as a function of the peak intensity I_0 in W/cm^2 for the two pulse shapes of Fig. 2: the Gaussian pulse with a solid line and the optimized shape with a dash-dotted line. The same ratios, but for probabilities averaged over the focal volume, are shown in the inset.

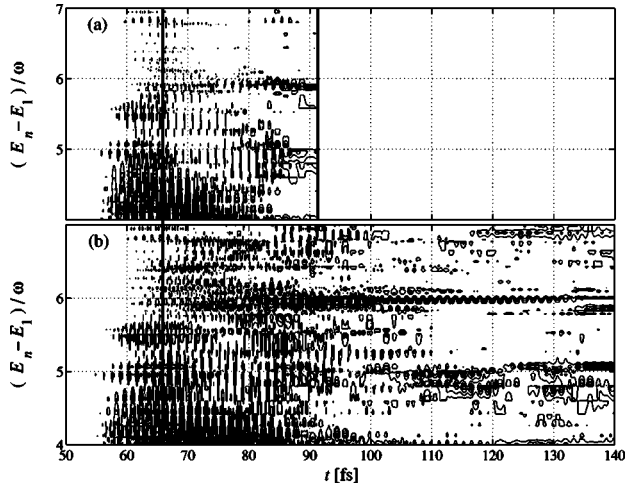

FIG. 6. Contour plots of the square of the coefficients of the wave packet $\Psi(x_1,x_2,t)$ in the expansion (12), $|c_n(t)|^2$, as functions of time t in fs and energy $(E_n-E_1)/\omega$, in units of photon energy. The time-dependent coefficients calculated with the Gaussian pulse are shown in panel (a), while panel (b) is for the optimized shape, with $I_0=4\times10^{12}$ W/cm^2. Note that the different total durations of the Gaussian and optimized pulses of Fig. 2 are also seen in the different time intervals of panels (a) and (b). The solid line at $t_p=64$ fs indicates the date of peak intensity in both panels while the right solid line in panel (a) shows the end of the Gaussian pulse.

The ratios of the averaged double- to single-ionization probabilities for the Gaussian and the optimized shapes are shown in the inset of Fig. 5. The enhancement of double ionization with the optimized pulse is confirmed, as seen in the experiment.

In order to understand the physics behind these optimizations it is informative to scrutinize the dynamics for each pulse shape by plotting the time-dependent populations of the eigenstates $P_n(t)=|c_n(t)|^2$ as functions of time t and energy E_n. These populations are shown in Fig. 6. The upper panel (a) pictures the excitation and ionization dynamics with the Gaussian shape, while the dynamics with the optimized pulse is shown in the lower panel (b). This figure shows these coefficients in the energy range $(E_1+4\hbar\omega \leq E_n \leq E_1+7\hbar\omega)$, corresponding to the absorption of 4 to 7 photons from the ground state. The eigenstates associated with these coefficients are therefore lying in between the two ionization thresholds, since $V^1_{\rm ion}\simeq 4\hbar\omega$ and $V^1_{\rm ion}+V^2_{\rm ion}\simeq 12\hbar\omega$. The peak intensity is here $I_0=4\times10^{12}$ W/cm^2.

It is clear from Fig. 6 that the ionization dynamics of the Ca atom is very similar when excited by the Gaussian or the optimized pulse at early times ($t \leqslant t_p = 64$ fs), but very different afterwards. Many more excited states are populated after the peak intensity when using the Ca^{2+} optimization. With this shape, the initial part of the pulse ($t \leqslant 80-90$ fs) prepares a coherent superposition of excited states. This superposition is then efficiently transferred into the double-electron continuum. Even though the Gaussian shape is characterized by a higher peak intensity, it does not carry as much energy as the optimized shape in the interval $t_p \leqslant t \leqslant t_f$, and therefore, does not induce efficient double ionization. The transient excited states seen in panel (b) could be either doubly excited states of Ca lying above the first ionization threshold or excited states of Ca^+. We will try, in the following Sec. III B, to determine their nature by performing single-active-electron (SAE) calculations. Indeed, SAE simulations should be able to reproduce the enhancement of double ionization if this enhancement proceeds sequentially with a transient production of Ca^+. On the contrary, if the electron correlations must be introduced in order to reproduce the optimization of double ionization, this enhancement is likely to involve one or a few doubly excited states.

B. Modeling the asymmetry

The obvious difference between the two laser-pulse shapes of Fig. 2 is the time asymmetry of the optimized pulse. To verify that this asymmetry is responsible for the optimization, we performed numerical simulations using simple model asymmetric pulse shapes whose widths τ_1 before $t = t_p$ differ from their widths τ_2 after t_p. These simple pulse shapes are made of two different $\sin^2$ wings: $f(t) = f_0 \sin^2(\pi t/2\tau_1)$ for $0 \leqslant t \leqslant t_p$, and $f(t) = f_0 \sin^2[\pi(t+\tau_2-\tau_1)/2\tau_2]$ for $t_p \leqslant t \leqslant t_f$. The date of peak intensity is here $t_p = \tau_1$, and the end of the pulse corresponds to $t_f = \tau_1 + \tau_2$. The amplitude parameter f_0 is adapted such that the total energy carried by the pulse remains constant when τ_1 or τ_2 vary. The asymmetry can then be characterized by the ratio $\gamma = \epsilon_2/\epsilon_1$ of the energy ϵ_2 carried by the pulse after t_p to its energy content before t_p: a value $\gamma < 1$ corresponds to $\tau_2 < \tau_1$ and therefore to a time asymmetry opposite to that observed in the Ca^{2+} optimization, a symmetric shape is obtained for $\gamma = 1$, and $\gamma > 1$ gives an asymmetry analogous to that of the optimization.

In the following simulations, we fix $\tau_2 = 20$ fs when $\gamma < 1$, and $\tau_1 = 20$ fs when $\gamma > 1$. Figure 7 shows two examples of these shapes with the asymmetry parameters $\gamma = 1$ in panel (a) and $\gamma = 2$ in panel (b). The resulting amplitude f_0 is shown as a function of γ in panel (c), and the maximum intensity is reached for the symmetric case $\gamma = 1$.

A naive guess for the variation of the ionization probability with the asymmetry parameter γ would be: the higher the peak intensity, the larger the ionization. In other words we could expect a global maximum of double ionization for the symmetric pulse ($\gamma = 1$). However, Fig. 8 demonstrates that the ionization of Ca is very sensitive to the asymmetry. This figure represents the double-ionization probability $W(Ca^{2+})$

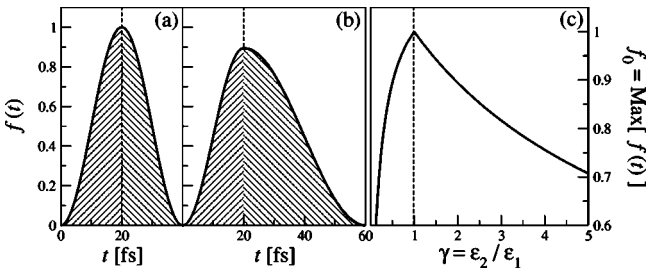

FIG. 7. Asymmetric laser pulse shapes $f(t)$ defined in Sec. III B as functions of time t in fs for two different values of the asymmetry parameter $\gamma = \epsilon_2/\epsilon_1$: $\gamma = 1$ in panel (a) and $\gamma = 2$ in panel (b). The variation of $f_0 = \mathrm{Max}[f(t)]$ with the asymmetry parameter γ is shown in panel (c) (see text for details).

calculated within the SAE (dash-dotted lines) and two-active-electrons (TAE, solid lines) approaches, as a function of the parameter γ. The upper curves (a) correspond to the intensity $I_0 = 3.75 \times 10^{12}$ W/cm^2, while the lower curves (b) were obtained at the intensity $I_0 = 2.87 \times 10^{12}$ W/cm^2. The single-active-electron calculations obviously do not include any electron correlations, and are similar to those described in Ref. [25], with soft-Coulomb parameters adjusted to reproduce the ionization potentials of Ca and Ca^+. Note that the left vertical scale refers to the TAE calculation, while the SAE probabilities should be read on the right side axis.

One can first note from the comparison of the SAE [right-hand side (rhs)] and TAE [left-hand side (lhs)] scales of this figure the huge enhancement, by four orders of magnitude, of double ionization when taking into account the electron correlations. The Coulomb repulsive force allows for energy transfer between the two electrons, and this acts in favor of ionization in situations where the two electrons are in an excited state. Even though it is not shown in this figure, the same trend is obtained for single ionization, and this corroborates some early experiments by DiMauro *et al.* [10],

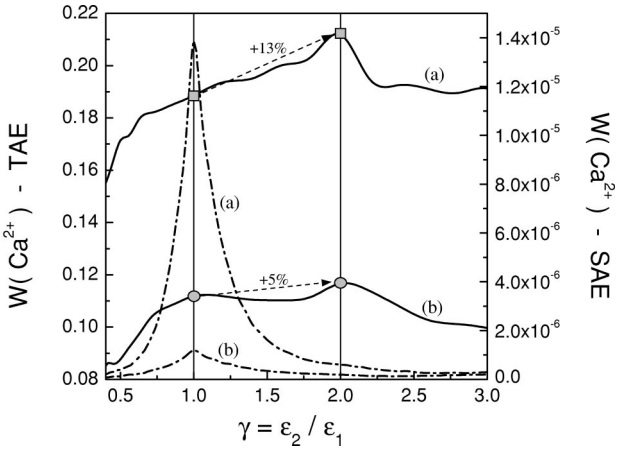

FIG. 8. Double-ionization probability $W(Ca^{2+})$ calculated using the two-active electron model (solid line) as well as using the single-active electron approximation (dash-dotted line) as a function of the asymmetry parameter γ. The lhs and rhs vertical scales are associated with the TAE and SAE probabilities, respectively. The peak intensity is fixed at $I_0 = 3.75 \times 10^{12}$ W/cm^2 for the two curves labeled (a), and at $I_0 = 2.87 \times 10^{12}$ W/cm^2 for the curves (b).

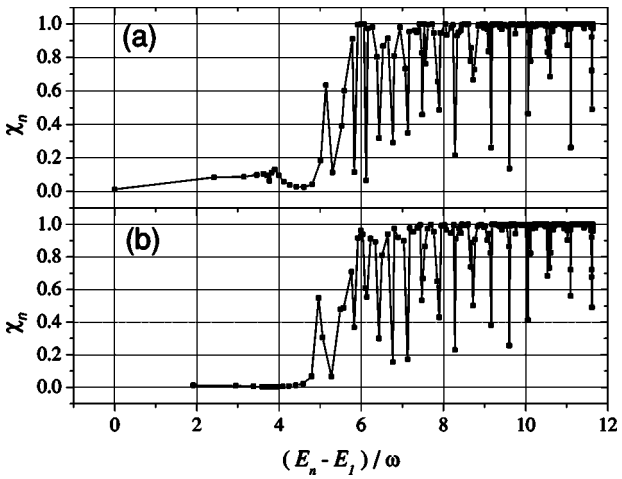

FIG. 9. Degree χ_n of double excitation of each bound and continuum eigenstate ψ_n as a function of energy $(E_n-E_1)/\omega$, in units of photon energy. Panel (a) corresponds to states of *gerade* symmetry, while panel (b) is for *ungerade* states. Doubly excited states are embedded in the continuum lying above the first ionization threshold ($\sim$4 photons), and are ordered in core-excited Rydberg series converging to higher thresholds [28].

who found that electron correlations play a significant role for the production of singly ionized Calcium.

Additionally, the SAE simulations follow the naive expectation described previously, and give a large global maximum of double ionization for $\gamma=1$. This maximum is shifted around $\gamma=2$ in the TAE calculation. This difference demonstrates that the electron correlation is the key to the optimization of double ionization in the adaptive control experiment [1]. The enhancement of the Ca^{2+} yield is therefore likely to proceed through some intermediate doubly excited states. The increase of the formation probability of Ca^{2+} when going from a symmetric to an asymmetric shape depends upon the intensity of the field. For example, this increase is of about 5% for the lowest intensity (2.87×10^{12} W/cm^2) shown Fig. 8, while it is of about 13% for the highest intensity (3.75×10^{12} W/cm^2). Of course, at much higher intensities the saturation regime is reached, and this phenomenon disappears. With the model $\sin^2$ pulse shapes used here, the enhancement of double ionization is not as impressive as with the optimized pulse, but nevertheless this effect is still significant enough to be compared with the results described in the previous Sec. III A using the experimental pulse shape.

In order to stress the role of doubly excited states in the optimization process, let us introduce the degree χ_n of double excitation of each bound and continuum eigenstate ψ_n [see Eq. (10)]

$$\chi_n=\sum_m |A_m^{(n)}|^2, \tag{20}$$

where the index m only spans doubly excited states, corresponding to $k>1$ and $l\geqslant k$ in Eq. (8). In Fig. 9, χ_n is plotted as a function of energy $(E_n-E_1)/\omega$, in units of photon energy. Note that the first and second ionization thresholds $V_{\rm ion}^1$ and $V_{\rm ion}^2$ roughly correspond to the absorption of 4 and 12 photons, respectively. This figure clearly shows that the eigenstates located around the six-photon transition are doubly excited ($\chi_n\simeq1$). Turning back to the optimization, we saw in Fig. 6 that these eigenstates are highly populated for $t>t_p$. This is a clear indication that the enhancement mechanism obtained experimentally proceeds through doubly excited states.

It should also be mentioned that the optimal value of the asymmetry parameter γ is found positive, as in the experiment, indicating that the left wing of the pulse shape ($t<t_p$) has to be shorter than the right wing ($t>t_p$). The origin of this phenomenon can be tentatively outlined as follows. As seen in Fig. 6, the states lying just above the first ionization threshold are excited relatively quickly, before the peak of the pulse. However, from this first step, the absorption of eight more photons is required to reach the second ionization threshold. In order to transfer this transient population into the double-ionization continuum, it is therefore preferable to ''stretch'' the pulse shape such that the intensity does not drop too quickly after $t=t_p$, even if this is done at the cost of lowering a bit the peak intensity of the pulse. The net result of the optimization is therefore to give a pulse shape which carries more energy after $t=t_p$, and this corresponds to $\gamma>1$.

IV. CONCLUSION

We have performed time-dependent simulations of the single and double ionization of atomic Calcium using a two-active-electron model. These simulations have been implemented within a basis set representation, allowing for an unambiguous calculation of the single- and double-ionization probabilities. The electron wave packet dynamics have revealed the main feature responsible for the enhancement of double ionization which was observed in a recent adaptive control experiment [1]: the time asymmetry of the laser-pulse envelope. During the ionization process, electron correlations play a decisive role, and doubly excited states serve as intermediate resonances.

The simulations show that the initial part of the pulse prepares a coherent superposition of excited states above the first ionization threshold. This superposition is ionized afterwards to produce Ca^{2+}. This second step is performed efficiently if the laser intensity does not drop too quickly after the peak of the pulse, and an asymmetric shape, with a slowly decreasing tail on the falling edge, therefore favors double ionization.

ACKNOWLEDGMENTS

We would like to thank Evangelos Papastathopoulos, Markus Strehle, and Gustav Gerber for very stimulating discussions, as well as for providing us with some experimental results prior to publication. We acknowledge a grant of computing time on the NEC SX-5 from the Institut de Développement et des Ressources en Informatique Scientifique (IDRIS) under Project No. 011459. This research was finan-

cially supported by the Ministère de la Recherche and by INTAS through the Grant No. 99-01495.

APPENDIX A: MAPPED COORDINATE

The integral (7) can be written in terms of the hypergeometric function ${}_2F_1$ as

$$p(x)=\frac{1}{\pi}\sqrt{\frac{2}{\alpha}}\left[x\times{}_2\mathrm{F}_1\left(\frac{1}{2},\frac{1}{4},\frac{3}{2};-\frac{x^2}{\alpha^2}\right)-x_0\right.$$
$$\left.\times{}_2\mathrm{F}_1\left(\frac{1}{2},\frac{1}{4},\frac{3}{2};-\frac{x_0^2}{\alpha^2}\right)\right]. \tag{A1}$$

From the Eq. (A1), it is easy to obtain $p(x)$ for the pure Coulomb potential ($\alpha=0$)

$$p(x)=\frac{2\sqrt{2}}{\pi}(\sqrt{|x_0|}+\mathrm{sgn}(x)\sqrt{|x|}). \tag{A2}$$

It should be noted that at small distances x, $p(x)$ is proportional to x when $\alpha\neq 0$, while in the case of the Coulomb problem $p(x)$ varies as $\sqrt{x}$.

APPENDIX B: MATRIX ELEMENTS OF THE HAMILTONIAN

Using the Dirac notations defined in Eq. (9), we write two basis set functions (8) as

$$\Phi_m=\begin{cases}\frac{1}{\sqrt{2}}(|k_1l_2\rangle+|k_2l_1\rangle) & \text{if } k\neq l\\ |k_1k_2\rangle \quad \text{otherwise,}\end{cases} \tag{B1a}$$

and

$$\Phi_n=\begin{cases}\frac{1}{\sqrt{2}}(|i_1j_2\rangle+|i_2j_1\rangle) & \text{if } i\neq j\\ |i_1i_2\rangle \quad \text{otherwise.}\end{cases} \tag{B1b}$$

The full Hamiltonian H_0 of Eq. (1) is a sum of single-electron Hamiltonians, and of the electron-electron interaction V_{12}. Using the orthonormalization relations of the single-electron wave functions φ_k, we then obtain the matrix elements of H_0 in the basis (8) as

$$\langle\Phi_n|H_0|\Phi_m\rangle=\langle\Phi_n|V_{12}|\Phi_m\rangle+E_{nm}, \tag{B2}$$

where

$$E_{nm}=\begin{cases}(\varepsilon_k+\varepsilon_l)(\delta_{ik}\delta_{jl}+\delta_{il}\delta_{jk}) & \text{if } i\neq j \text{ or } k\neq l\\ 2\varepsilon_k\delta_{ik} \quad \text{otherwise.}\end{cases} \tag{B3}$$

It should be mentioned that due to the spatial symmetry of the Hamiltonian (1) the eigenfunctions (10) with a given symmetry (*gerade* or *ungerade*, see text for details) are expanded over the basis set functions (8) showing the same symmetry

$$\psi_n^{(g,u)}(x_1,x_2)=\sum_m A_m^{(n)}\Phi_m^{(g,u)}(x_1,x_2), \tag{B4}$$

where the superscripts (g) and (u) denote the *gerade* and *ungerade* symmetries, respectively. Hence, the matrix elements (B2) of the Hamiltonian (1) can be calculated separately for the two different symmetries.

APPENDIX C: DIPOLE MATRIX ELEMENTS

Using the notations defined in Eq. (9), the calculation of the dipole matrix elements $D_{nm}=\langle\Phi_n|\mu|\Phi_m\rangle$ gives

$$\begin{aligned}
-(x_{ik}\delta_{jl}+x_{il}\delta_{jk}+x_{jk}\delta_{il}+x_{jl}\delta_{ik}) &\quad \text{if } i\neq j \text{ and } k\neq l,\\
-\sqrt{2}(x_{il}\delta_{ik}+x_{ik}\delta_{il}) &\quad \text{if } i=j \text{ and } k\neq l,\\
-\sqrt{2}(x_{ik}\delta_{jk}+x_{jk}\delta_{ik}) &\quad \text{if } i\neq j \text{ and } k=l,\\
-2x_{ik}\delta_{ik} &\quad \text{if } i=j \text{ and } k=l,
\end{aligned} \tag{C1}$$

where the notation x_{ik} denotes the one-dimensional integral

$$x_{ik}\equiv\langle i|x|k\rangle. \tag{C2}$$

[1] E. Papastathopoulos, M. Strehle, and G. Gerber (unpublished).

[2] *Multiphoton Processes*, edited by P. Lambropoulos and H. Walther (Institute of Physics Publishing, University of Reading, Berkshire, 1997).

[3] *Multiphoton Processes*, edited by L. F. DiMauro, R. R. Freeman, and K. C. Kulander (American Institute of Physics Publishing, N.Y., 2000).

[4] D.N. Fittinghoff, P.R. Bolton, B. Chang, and K.C. Kulander, Phys. Rev. Lett. **69**, 2642 (1992).

[5] B. Walker, B. Sheehy, L.F. DiMauro, P. Agostini, K.J. Schafer, and K.C. Kulander, Phys. Rev. Lett. **73**, 1227 (1994).

[6] J.B. Watson, A. Sanpera, D.G. Lappas, P.L. Knight, and K. Burnett, Phys. Rev. Lett. **78**, 1884 (1997).

[7] D. Bauer, Phys. Rev. A **56**, 3028 (1997).

[8] D.G. Lappas and R. van Leeuven, J. Phys. B **31**, L249 (1998).

[9] P. Agostini and G. Petite, J. Phys. B **17**, L811 (1984).

[10] L.F. DiMauro, K. Dalwoo, M.W. Courtney, and M. Anselment, Phys. Rev. A **38**, 2338 (1998).

[11] S. Shi, A. Woody, and H. Rabitz, J. Chem. Phys. **88**, 6870 (1988).

[12] A. Peirce, M. Dahleh, and H. Rabitz, Phys. Rev. A **37**, 4950 (1988).

[13] R. Kosloff, S. Rice, P. Gaspard, S. Tersigni, and D.J. Tannor, Chem. Phys. **139**, 201 (1989).

[14] R.S. Judson and H. Rabitz, Phys. Rev. Lett. **68**, 1500 (1992).
[15] T. Baumert, T. Brixner, V. Seyfried, and G. Gerber, Appl. Phys. B: Lasers Opt. **B65**, 779 (1997).
[16] C.J. Bardeen, V.V. Yakovlev, K.R. Wilson, S.D. Carpenter, P.M. Weber, and W.S. Warren, Chem. Phys. Lett. **280**, 151 (1997).
[17] A. Assion, T. Baumert, M. Bergt, T. Brixner, B. Kiefer, V. Seyfried, M. Strehle, and G. Gerber, Science **282**, 919 (1998).
[18] T. Brixner, M. Strehle, and G. Gerber, Appl. Phys. B: Lasers Opt. **B68**, 281 (1999).
[19] J.Y. Eberly, R. Grobe, C.K. Law, and Q. Su, *Atoms in Intense Laser Fields* (Academic, N.Y., 1992), p. 301.
[20] R. Kosloff, *Dynamics of Molecules and Chemical Reactions* (Marcel Dekker, New York, 1996), p. 185.
[21] E. Fattal, R. Baer, and R. Kosloff, Phys. Rev. E **53**, 1217 (1996).
[22] V. Kokoouline, O. Dulieu, R. Kosloff, and F. Masnou-Seeuws, J. Chem. Phys. **110**, 9865 (1999).
[23] J.H. Verner, SIAM (Soc. Ind. Appl. Math.) J. Numer. Anal. **15**, 618 (1978).
[24] N.B. Delone and V.P. Krainov, *Multiphoton Processes in Atoms* (Springer, New York, 2000).
[25] A. Pegarkov, E. Charron, and A. Suzor-Weiner, J. Phys. B **32**, L363 (1999).
[26] E.A. Volkova, A.M. Popov, and O.V. Tikhonova, J. Exp. Theor. Phys. **87**, 875 (1998).
[27] J.D. Jackson, *Classical Electrodynamics* (Wiley, New York, 1998).
[28] G. Tanner, K. Richter, and J. Rost, Rev. Mod. Phys. **72**, 497 (2000).